Preliminary deformation detection of high-fill sections along the Inuvik-Tuktoyaktuk Highway using UAV photogrammetry

Dylan M.J. Stafford, Earl Marvin B. De Guzman, Samuel W. Kaluzny, Marolo C. Alfaro
Department of Civil Engineering – University of Manitoba, Winnipeg, MB, Canada
Lukas U. Arenson
BGC Engineering Inc., Vancouver, BC, Canada
Guy Doré
Université Laval, Laval, QC, Canada

ABSTRACT
The Inuvik-Tuktoyaktuk Highway (ITH) is a newly constructed highway in Northwest Territories, Canada in the continuous permafrost zone. The 137 km-long two-lane gravel surface road was constructed during winter using locally-available fill material with no cuts into the ground to minimize disturbance of the permafrost foundation. The embankment thicknesses were designed to provide insulation to the underlying permafrost as well as to maintain road geometry requirements. However, high-fill sections ranging from 5 to 12 m are susceptible to deformation in the form of settlements and slope movements. As part of an on-going research program studying the performance of embankments in Arctic regions, deformation of two high-fill sections along ITH were monitored using an unmanned aerial vehicle (UAV) and photogrammetric processing. Aerial images of the two sections were obtained in August 2017 and August 2018. Images were processed using structure-from-motion (SfM) software and the annual embankment deformations of each section were detected using two cloud comparison methods: cloud-to-mesh (C2M) and multiscale model-to-model cloud comparison (M3C2). C2M and M3C2 produced comparable results for both sections. This paper presents the detected deformations of the two sections, the challenges encountered during data acquisition and processing, and recommended best practices in using UAVs for monitoring deformations.

RÉSUMÉ
La Inuvik-Tuktoyaktuk Highway (ITH) est une route nouvellement construite dans les Territoires du Nord-Ouest, au Canada, dans la zone de pergélisol continu. La route de gravier à deux voies de 137 km de long a été construite en hiver à l'aide de matériaux de remblai disponibles localement, sans coupures dans le sol, afin de minimiser la perturbation de la fondation de pergélisol. Les épaisseurs des remblais ont été conçues pour isoler le pergélisol sous-jacent et pour maintenir les exigences de géométrie de la route. Cependant, les sections de remblayage élevées allant de 5 à 12 m sont susceptibles de se déformer sous la forme de tassement et de mouvement de la pente. Dans le cadre d'un programme de recherche en cours visant à étudier les performances des remblais dans les régions arctiques, la déformation de deux tronçons à remplissage élevé le long de ITH a été surveillée à l'aide d'un véhicule aérien sans pilote (UAV) et d'un traitement photogrammétrique. Les images aériennes des deux sections ont été obtenues en août 2017 et août 2018. Les images ont été traitées à l'aide du logiciel SfM (structure par mouvement) et la déformation annuelle du remblai de chaque section a été détectée à l'aide de deux méthodes de comparaison de nuage: nuage à maillage (C2M) et la comparaison multi-échelles de nuage de modèle à modèle (M3C2). C2M et M3C2 ont produit des résultats comparables pour les deux sections. Ce document présente les déformations détectées dans les deux sections, les difficultés rencontrées lors de l'acquisition et du traitement des données, ainsi que les meilleures pratiques recommandées pour l'utilisation des UAV pour la surveillance des déformations.

1 INTRODUCTION

Embankments in Arctic regions are usually constructed during winter to improve mobility of construction equipment on the frozen ground and minimize disturbance of permafrost by reducing heat input to the ground. These embankments are often constructed on difficult ground conditions such as thaw-sensitive and ice-rich soils, and their structural stability can be challenging to maintain. Frozen embankment fill material can have a high ice content, which can lead to instabilities as the ice melts in the summer following construction. Another common cause of embankment instability and deformation is progressive thawing of foundation soil at the toe. Snow drifts that build up at embankment toe during winter provide insulation and prevent the ground from refreezing. The thawed zone then extends further beneath the embankment as the foundation soil thaws the next summer. Large thaw zones can develop at the toe as this cyclic process continues, causing subsidence of the toe and an outward movement of the slope. This can lead to longitudinal cracking along the embankment road surface and slope failures in extreme cases. The warming climate is exacerbating embankment instability issues associated with degrading permafrost, and research is needed to better understand and predict how embankments in the Arctic will perform in the future.

The Inuvik-Tuktoyaktuk Highway (ITH) is a newly-constructed highway in Northwest Territories, Canada that was opened to the public in November, 2017. The 137 km-

long two-lane gravel surface road is located above the Arctic Circle in the continuous permafrost zone. A peat layer at ground surface up to 7 m thick covers most of the region, with soil in the permafrost beneath containing excess ice in the form of ice veins, lenses, wedges, and massive ice (Rampton, 1988). ITH was constructed during winter using locally-available fill materials with no cuts into the ground, 3:1 sideslopes, and a minimum thickness of 1.8 m. Embankment fill material was sourced locally and consisted primarily of silt, sand, and gravel from glacial deposits. Several high-fill sections were constructed in order to maintain safe vertical alignments through the complex thermokarst terrain. These high-fill sections are more susceptible to slope movements and deformations, making them critical sections to monitor and study. One high-fill section at KM 82 was reinforced with wicking geotextiles as part of a larger research project. Shape Accel Arrays (SAA) were installed in the reinforced section and a non-reinforced control section to measure displacements in the embankment.

This research work used an unmanned aerial vehicle (UAV) to detect deformations and monitor the performance of high-fill sections along ITH. SAA data was used to check the deformations detected by the UAV. Aerial images were captured by the UAV and processed using an advanced class of photogrammetric algorithms known as structure-from-motion (SfM). SfM performs a series of automated image matching and calibration algorithms on a set of images with a high degree of overlap that capture the full three-dimensional (3D) scene from a wide array of positions. The camera pose and scene geometry are solved simultaneously using a highly-redundant bundle adjustment based on matching features in multiple images (Westoby et al. 2012). The product of SfM processing is a dense 3D point cloud of the captured scene, which can be used to monitor deformation when periodic UAV surveys of the same scene are conducted. The quality of the reconstruction is highly dependent on the image resolution and scale, image network geometry, surface texture, lighting conditions, and control point characteristics (Westoby et al. 2012; Eltner et al. 2016). UAV flights were carefully planned to optimize the quality of the resulting reconstruction.

Two methods were used to measure deformation between point clouds; namely, cloud-to-mesh (C2M) and multiscale model-to-model cloud comparison (M3C2; Lague et al. 2013). C2M involves creating a detailed 3D meshed surface of the reference point cloud using the Poisson Surface Reconstruction algorithm by Kazhdan et al. (2006) and calculating the distance along the mesh surface normal to the compared point cloud. On projects such as this where deformations are not restricted to the vertical direction, distance measurements along surface normals are easier to interpret than strictly vertical deformations, which often overestimates actual change (Abellan et al. 2014). One limitation of C2M is that some details in surface roughness are lost during the mesh interpolation. This can limit small-scale change detection. M3C2 is a more advanced method for measuring distances between clouds that was developed on three key characteristics: 1) operates directly on point clouds without meshing or gridding; 2) computes the local distance along the normal surface direction; and 3) estimates a level of detection (LoD) for each distance measurement based on local point cloud roughness and registration error. M3C2 surface normals can be calculated on multiple scales to determine the most planar normal surface and the algorithm can be executed on a subsample of the original point cloud in order to save time (Lague et al. 2013). Stumpf et al. (2015) found lower error measurements with M3C2 compared to C2M. Comparisons of M3C2 to C2M also demonstrated that M3C2 was superior in measuring small-scale deformations over time and was a more accurate measurement of true change (Barnhart and Crosby 2013).

2 METHODOLOGY

2.1 Site Description

This research focused on two high-fill sections of ITH, located at KM 82 and KM 118. KM 82 is a 120 m-long section that is 6 m high. A toe berm was constructed on the east side of the embankment to improve stability of the sideslope. KM 118 is a 200 m-long section that transects a deep valley. The embankment is symmetrical and 12 m thick at its highest point, making it the thickest embankment section of ITH.

2.2 Flight Planning

The UAV used for this research was the senseFly albris. The albris has a 38 Mp main camera and a global positioning system (GPS) that allows it to fly autonomously on user-designed missions, making it highly effective for mapping and inspection. eMotion 3 (senseFly 2018) is the mission planning software that was used to design UAV flights. It was recommended in literature that flights should follow horizontal grid paths and capture vertical, parallel-axis images with a high degree of overlap at consistent spacing because uniform coverage of the scene is effective for aerial photogrammetric reconstruction (James and Robson 2014). A high degree of image overlap is important so that features are visible in many images and large amounts of keypoints can be matched. An overlap of 75% (both longitudinal and lateral with the UAVs flight path) was selected for all grid flights. Another important parameter for UAV surveys is the ground sampling distance (GSD; i.e. distance between pixel centers measured on the ground). Decreasing the camera-to-surface distance increases the GSD and the spatial resolution of the image, enhancing the spatial density of keypoints and increasing the resolution of the point cloud (Westoby et al. 2012). GSD was set to 1 cm for all grid flights, providing sufficient spatial resolution and accounting for battery life of the UAV.

A drawback of grid flights is the systematic vertical doming error that can develop during processing. Systematic doming results in point clouds where the centre of the reconstruction is incorrectly computed to be at a higher elevation than the edges, which appear stretched downwards. It occurs due to the self-calibration of camera parameters during the SfM bundle adjustment of parallel-axis imagery (Fonstad et al. 2013; James and Robson

2014; Eltner et al. 2016). Reconstructions can achieve cm-scale accuracy and still contain large vertical doming errors of the surface (James and Robson 2014). These doming errors can be reduced by up to two orders of magnitude by including oblique images in the survey (James and Robson 2014). Therefore, a set of oblique images were collected, in addition to the nadir grid images, to minimize vertical errors in the point clouds. Oblique flights were designed as a point of interest (POI) mission, with the POI being at the centerline of the road surface in the middle of the zone. A POI mission included 12 images captured at 45° angles from vertical, as per recommendations by James and Robson (2014).

Point clouds reconstructed by SfM processing are generated in an arbitrary coordinate system. To confidently compare point clouds from different epochs and detect deformations, point clouds must be georeferenced to the same coordinate system. The most common method for georeferencing UAV image-derived point clouds is by surveying ground control points (GCPs). This research used the Leica GS14+CS20 real-time kinematic (RTK) global navigation survey system (GNSS) to measure coordinates of checkerboard GCPs. The checkerboards were were 60 cm x 60 cm plywood pieces, spray-painted in bright colours to be easily identifiable. Precise GCP coordinates were imported during image processing and a 3D Helmert transformation with 7 parameters (3 translations, 3 rotations, and 1 scale) transformed the point cloud from an arbitrary coordinate system into a real-world coordinate system.

A minimum of 3 GCPs is required for georeferencing, but increasing the number of GCPs provides a more robust solution that is less sensitive to error at any one point and generally reduces georeferencing errors (James and Robson 2012). Several researchers have investigated how the number of GCPs affects the accuracy of UAV image-derived point clouds. Tahar (2013) found 8 GCPs to be the most accurate for surveying a road construction site. Pix4Dmapper (Pix4D 2018), the SfM photogrammetry software use for data processing in this research, recommends to use between 8 and 12 GCPs. We settled on using 10 GCPs. GCPs were distributed widely across the study area to reduce overall errors by providing uniform coverage (Eltner et al. 2016) and were located slightly outside the embankments to ensure coordinate transformations were not being extrapolated outside the volume encompassed by the control points (James and Robson 2012).

2.3 Site Visits and Data Acquisition

Images and data for deformation detection was acquired on two site visits: August 2017 and August 2018. One grid flight was conducted at each section in 2017. Prior to any UAV flights in 2018, base station control was established at both high-fill sections. Natural Resources Canada's Precise Point Positioning web service was used to analyze base station GNSS data and provide exact coordinates of metal rods hammered deep into the ground. The base station could now be set up at the same location with precise known coordinates for all surveys at that section, allowing for more accurately georeferenced reconstructions. Two flights were conducted at KM 82 in 2018: a grid flight and a POI flight. At KM 118 in 2018, only a grid flight was conducted because weather conditions did not permit time for a POI flight. 10 GCPs were used for the surveys.

2.4 Data Analysis

Image processing and the SfM workflow was executed using Pix4Dmapper. The general workflow in Pix4D was as follows. First, initial processing of the point cloud was performed, which included identification of keypoints, keypoints matching between images, and a bundle adjustment to orient the keypoints and create a sparse point cloud. The full scale of the images were processed with no down-sampling to maximize the number and accuracy of keypoints (Harwin and Lucieer 2012). The GCP coordinate data, which was originally processed using Leica Infinity (Leica Geosystems 2018), was imported to Pix4D and each GCP was marked in all images it was visible in. Marking GCPs in the images themselves reduces errors and improves overall accuracy compared to marking GCPs in the point cloud (Eltner et al. 2016). The point cloud was then reprocessed to include GCP coordinates in the bundle adjustment (i.e. a 1-stage bundle adjustment), which has been shown to reduce systematic doming errors (Eltner et al. 2016). Once the sparse point cloud was georeferenced, advanced computer vision algorithms were performed to densify the point cloud. Figure 1 shows the acquired images and dense point cloud for the 2018 flights at KM 82. Dense point clouds were exported from Pix4D and used in other software to measure deformation through cloud comparisons.

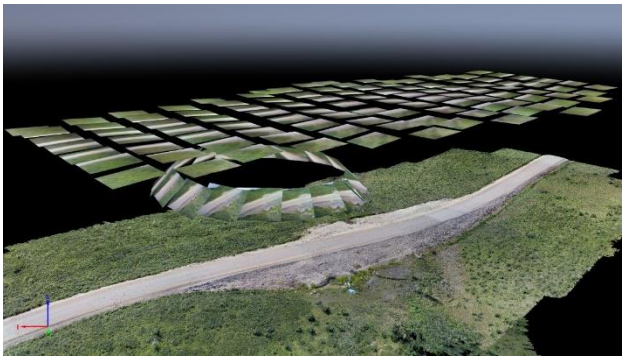

Figure 1. Captured images and reconstructed point cloud for KM 82 (2018) in Pix4Dmapper

Comparison of the 2017 and 2018 point clouds to detect annual surficial deformations of the high-fill sections was performed in the open-source software CloudCompare (2018). The first step was registration of the reference point cloud (2017) and compared point cloud (2018) by executing iterative closest point (ICP), a commonly-used least-squares matching algorithm. This registration would not have been necessary if the 2017 points clouds were accurately georeferenced. In situations where there are stable areas of a point cloud that aren't deforming and unstable areas that are (e.g. rockfall monitoring), unstable

areas can be temporarily removed and the point clouds can be registered based on the stable areas (Gruen and Acka 2005; Meeks et al. 2017). For the high-fill sections along ITH, no areas were certainly stable due to possible settlement and slope movements, which added a source of uncertainty to the registration process. The highway was also resurfaced with approximately 300 mm of compacted gravel between the 2017 and 2018 surveys, further complicating registration. To address this, the road surface was temporarily cut from the point clouds for registration, then added back into the registered point clouds.

C2M distance measurement involved generating a mesh surface of the reference point cloud through the Poisson surface reconstruction algorithm (Kazhdan et al. 2006), calculating surface normals, and computing distances along the surface normal from the reference mesh to the compared point cloud. M3C2 did not require meshing and was performed directly on the point clouds. Both cloud comparison methods require the definition of a few key parameters to maximize their efficacy. M3C2 requires projection scale (*d*) for surface roughness estimates, normal scale (*D*) for normal direction calculation, and core point spacing (*s*) for subsampling the point clouds. Guidance for selecting the parameters was provided by Lague et al. (2013). Preliminary M3C2 computations were run as sensitivity analyses to optimize parameters for each point cloud. C2M only requires *D*, and the optimal *D* for each point cloud using M3C2 was also assigned as *D* for C2M. The LoD for a 95% confidence interval, which is commonly used in change detection applications, is calculated for M3C2 as:

$$LoD = \pm 1.96\left(\sqrt{\frac{\sigma_1^2}{n_1} + \frac{\sigma_2^2}{n_2}} + reg\right) \quad [1]$$

where η is the number of points used to calculate the standard deviation of points in the normal direction, σ and *reg* is the registration error between point clouds. Local surface roughness parameters (η and σ) is computed based on the point clouds, but *reg* must be manually defined. The following procedure to calculate *reg* was based on recommendations by Eltner et al. (2016). The bundle adjustment in Pix4D was performed with one GCP left out of the calculations and the calculated position of that GCP was compared to its actual position to determine positional errors. This was repeated for each of the 10 GCPs, and the global root mean-squared error (RMSE) of all 10 GCPs was determined for each survey. For a given deformation analysis between two epochs, *reg* is calculated as:

$$reg = \sqrt{RMSE_{2017}{}^2 + RMSE_{2018}{}^2} \quad [2]$$

The value of *reg* was determined to be 63 mm for KM 118. For KM 82 where there were no GCPs used in 2017 and therefore no RMSE estimate, *reg* was taken to be 20 mm ($RMSE_{2018}$). Core point spacing of 10 mm was used for all M3C2 comparisons. The optimal point cloud parameters for each reconstruction are provided in Table 1.

Table 1. Optimized M3C2 and C2M parameters

Survey	RMSE (mm)	d (mm)	D (mm)
KM 82 2017	-	13	300
KM 118 2017	58	13	300
KM 82 2018	20	12	400
KM 118 2018	24	16	500

3 RESULTS

3.1 KM 82 Deformation

Deformation at KM 82 was computed using C2M (Figure 2) and M3C2 (Figure 3), and compared to confirm that C2M and M3C2 provided similar results. Note that in all C2M and M3C2 deformation figures, values are displayed in metres and the scale is from -0.3 m to 0.3 m. C2M and M3C2 produced comparable results for both sections. The results showed subsidence of approximately 100 mm at the mid-slope and toe, likely caused by thaw compression of the permafrost foundation. Positive change was detected along the road surface due to the resurfacing that occurred. The extreme positive change at the edges of the reconstruction was not actual deformation of the embankment. Rather, it was the manifestation of a systematic doming error that occurred in the 2017 point cloud that caused incorrect positive change to be measured at the edges. This occurred because the 2017 flight was conducted before the GCP checkerboards were delivered to site and the reconstructed point cloud was not properly georeferenced.

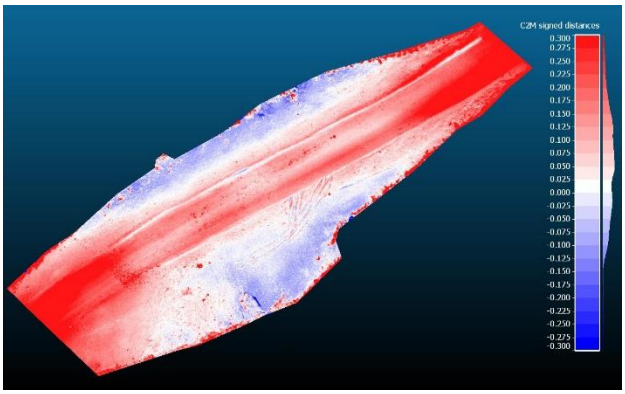

Figure 2. KM 82 C2M deformation

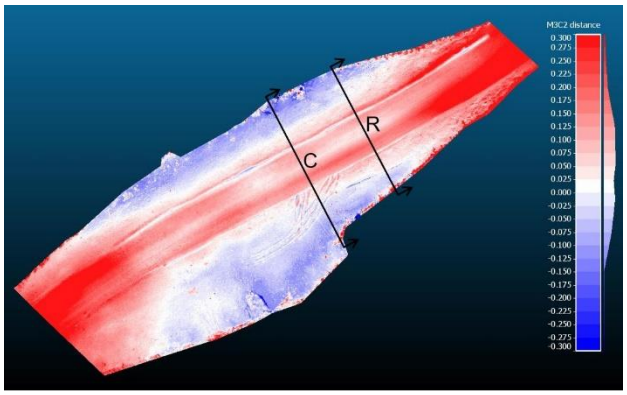

Figure 3. KM 82 M3C2 deformation with control (C) and reinforced (R) cross-section lines

Cross-sections of the reinforced and control sections (Figures 4 and 5) were extracted as slices from the 2017 and 2018 point clouds. Sections were located at the SAAs to allow for a direct comparison to the SAA data. Due to the difference in magnitude between the size of embankment and the measured deformation, deformations for the cross-section comparisons were exaggerated 2x at KM 82 to allow for better visual analysis. The results showed that deformation at mid-slope above the SAAs were minimal compared to the road surface and toe.

Based on the available data, LoD estimates for the KM 82 M3C2 computation ranged between 40 and 50 mm. However, this underestimates the true LoD because the 2017 survey did not include GCPs and *reg* only accounted for the 2018 GCP errors. The SAAs at both the control and reinforced sections measured approximately 50 mm of settlement between August 2017 and August 2018. The top nodes of the SAAs are located roughly 400 mm below the sideslope surface and the data can be extrapolated to expect approximately 60 mm of settlement at the surface above the instruments. UAV-measured surficial deformations cannot be validated by the SAA data based only on the one year of data because the actual deformation measured by the SAAs is not significantly larger than the LoD. Future UAV monitoring of the embankment with comparison to the SAA data is required to validate the deformations detected by the UAV.

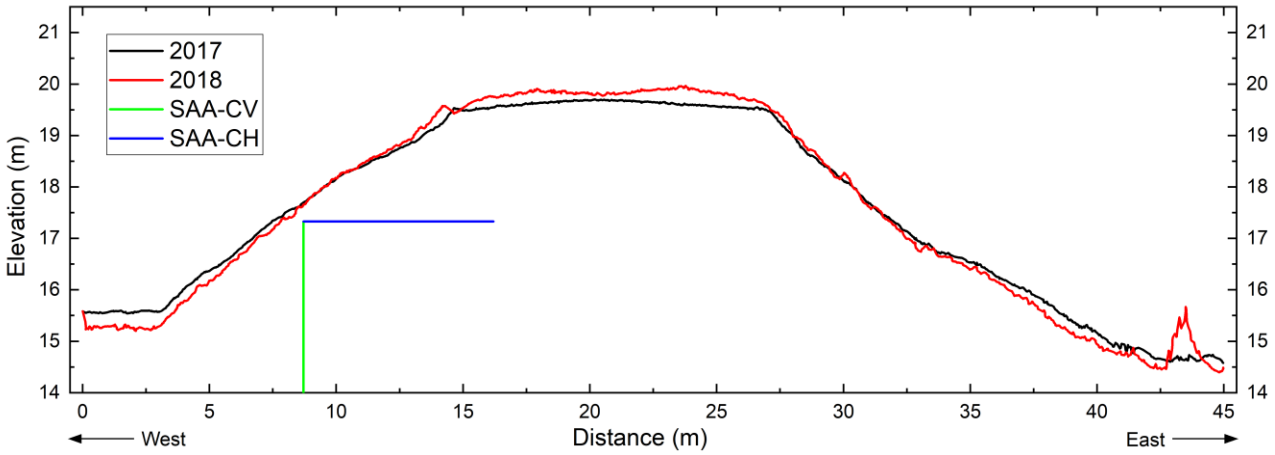

Figure 4. KM 82 cross-section deformation at the control section

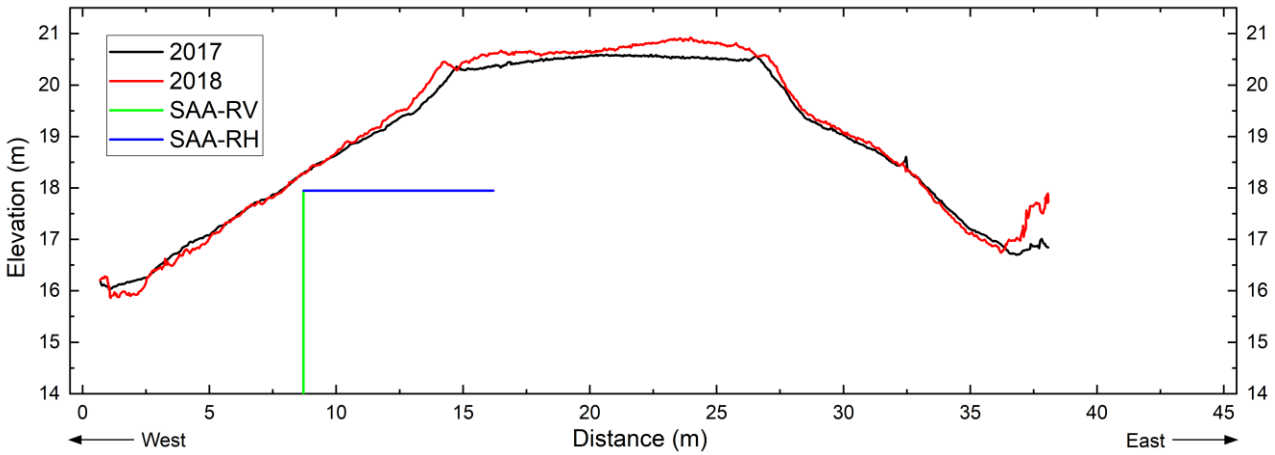

Figure 5. KM 82 cross-section deformation at the reinforced section

3.2 KM 118 Deformation

Deformation measurements for KM 118 using M3C2 (Figure 6) showed negative change at the upper-slope of approximately 50 mm and positive change at the lower-slope of 80-120 mm. It is hypothesized that this lateral spreading of material at the lower-slope was caused by the thawed embankment soil having too low of a shear strength to resist deforming under the mass of upper slope material. The lateral spreading behaviour was detected on both sideslopes, but was more distinct on the west slope. Relatively large amounts of vegetation growth were detected on sideslopes at KM 118 compared to KM 82, which was represented as positive change greater than 300 mm. GCPs are supposed to encompass the entire survey area (James and Robson 2012), but for the 2018 survey the GCPs were clustered near the middle of the high-fill section. The negative change of 100 mm at the north and south extents was not actual deformation, but instead it was the manifestation of a minor doming error that occurred outside the area of GCP coverage.

Cross-sections approximately 20 m south of the culvert were extracted from the 2017 and 2018 point clouds for comparison (Figure 7). Deformation for the cross-section comparison was exaggerated 3x at KM 118. The cross-section comparison highlighted the lateral spreading behaviour that is occurring at the lower-slope on the west. LoD estimates for the KM 118 M3C2 computation ranged between 125 and 135 mm. This relatively large LoD was caused by the weak GCP survey of 2017 having an RMSE of 58 mm. The magnitude of the LoD relative to the small range of values indicates that the LoD is mostly controlled by *reg* (refer to Equation 1). GCP RMSE must be reduced in future surveys in order to reduce the LoD and accurately measure small-scale deformations of the high fill sections. Approaches to reduce GCP errors are discussed in Section 4.

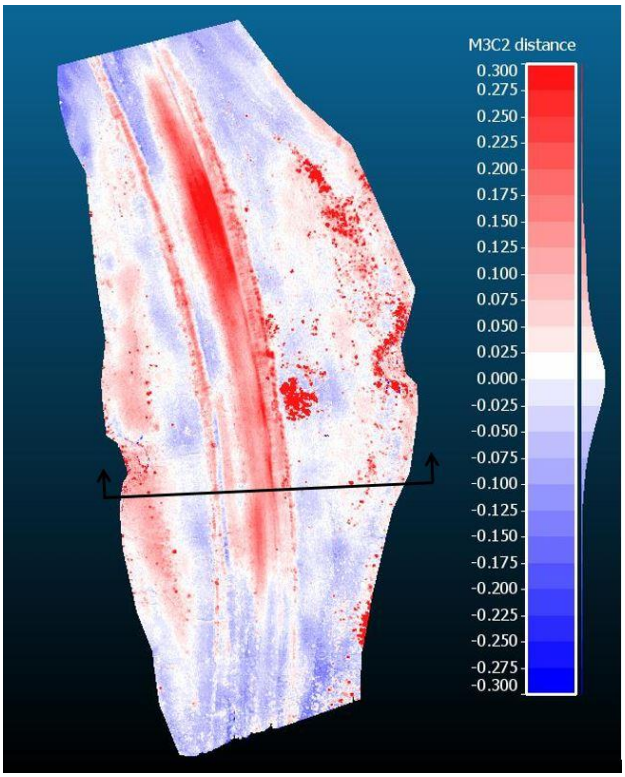

Figure 6. KM 118 M3C2 deformation with cross-section line

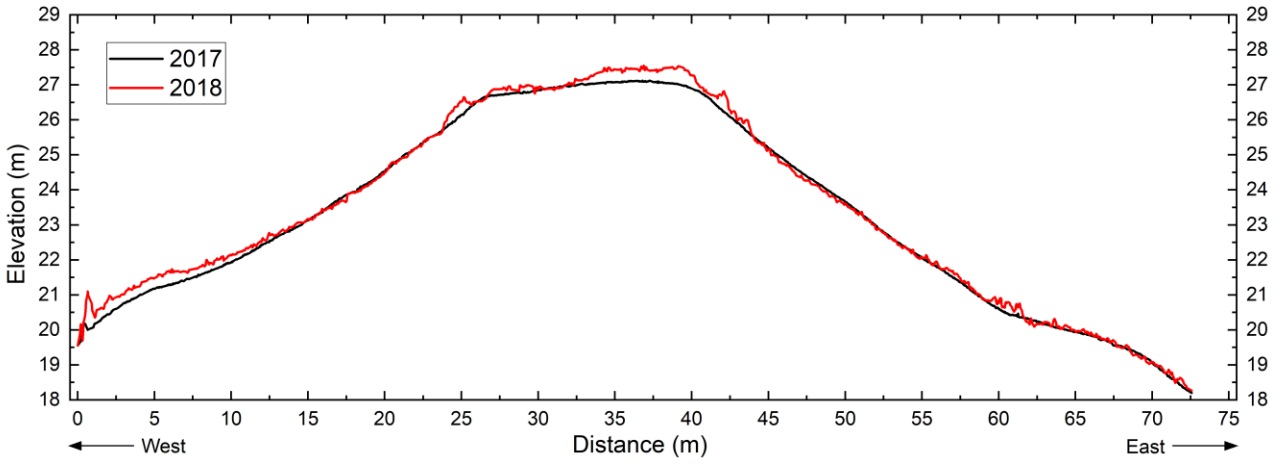

Figure 7. KM 118 cross-section deformation

4 DISCUSSION

C2M and M3C2 distance calculations provide evidence that the high-fill sections at KM 82 and KM 118 are deforming. The lower-slope subsidence and lateral spreading detected at the two high-fill sections has not impacted the overall structural stability of the embankment. It will be interesting to study future deformation results to quantify how the rate of movement is changing. The surficial deformation results could supplement numerical modelling of the high-fill sections by providing a deformation measurement for comparison. Coupling numerical modelling with the UAV photogrammetry deformation detection could be an effective approach to better understand the behavior of embankments in the Arctic.

Georeferencing issues from the 2017 surveys led to challenges during the registration process and higher uncertainty in the deformation measurements. The major issue with the 2017 and 2018 surveys is that they weren't georeferenced to the same local coordinate system. Registration by the ICP algorithm presented a reasonable approach to align the point clouds, although there were inevitable errors due to deformation that occurred. The 2018 point clouds may have been shifted or tilted slightly incorrectly, which would have influenced the measured deformation. Fortunately, precise local coordinate systems were established for both sections during the 2018 site visit and all surveys that year were georeferenced to these coordinate systems. Future UAV surveys will be georeferenced to the same coordinate systems, which will significantly improve precision of registrations. To eliminate the systematic doming errors that were observed at both sections, GCP coverage will be extended to encompass the entire high-fill section of the embankment. Other techniques to reduce GCP error, such as longer data collection times at each GCP, are being investigated and will be implemented on future site visits.

Techniques to improve UAV image acquisition can also be implemented to reduce reconstruction errors. Including a POI flight at KM 82 in 2018 was effective at reducing GCP errors. The GCP RMSE was 53 mm if only the grid flight images were included in processing and 20 mm when additional POI images were included. A 33 mm GCP error reduction will translate to a significantly lower LoD. Therefore, POI imagery is highly recommended for future flights. The exact geometry of POI flights will be investigated so that it can be optimized for future site visits. Increasing the number of GCPs per section should also reduce the GCP RMSE, which will also be investigated. Another technique would be to lower the elevation at which the UAV flies on the grid flights. This would reduce the GSD and increase accuracy of the reconstruction. A downside of flying the UAV lower is that more battery will be used. Either a smaller section of the embankment would be surveyed or two UAV flights would need to be performed. The goal of these GCP and UAV method improvements is to reduce errors in the reconstruction and allow for more accurate deformation detection.

5 CONCLUSION

Deformations of two high-fill sections (KM 82 and KM 118) along ITH were monitored using a UAV and photogrammetric processing. Images were processed using SfM software to produce dense point clouds, and the annual embankment deformation of each section was detected using two cloud comparison methods: C2M and M3C2. Instrumentation was installed in the high-fill section at KM 82 to measure displacements in the embankment. At KM 82, the UAV detected subsidence at the mid-slope and toe, and minor deformation at the upper slope. UAV-measured deformation cannot be validated by the instrument data based only on the one year of data because the actual deformation measured by the SAAs is insignificantly larger than the estimated LoD. Future UAV monitoring of KM 82 with comparison to the SAA data is required to validate the deformations detected by the UAV. The thickest embankment section at KM 118 exhibited a lateral spreading behaviour at the lower-slope that was likely caused by the thawed embankment soil having too low of a shear strength to resist movements under the mass of upper slope material.

Georeferencing issues in 2017 led to difficulties during registration of point clouds and higher levels of uncertainty for the deformation measurements. Georeferencing issues also caused systematic doming errors in the point clouds. A few techniques will be used to improve the quality of GCP measurements: 1) georeferencing to an established local coordinate system; 2) increase the number of GCPs per section; 3) larger GCP coverage of the high-fill sections; and 4) longer data collection times for GCPs. Changes to the UAV image geometry will also be implemented to further reduce errors and improve overall precision of the reconstructions. Implementing these techniques will eliminate systematic errors in the point clouds, increase the spatial resolution and accuracy of the point clouds, and allow for more precise registration, ultimately producing more accurate deformation measurements.

6 ACKNOWLEDGEMENTS

This research work was funded by the Department of Infrastructure of the Government of Northwest Territories (GNWT DOI), Transport Canada (TC), and the Natural Sciences and Engineering Research Council (NSERC). The authors would like to acknowledge the field engineers of GNWT DOI for their on-site coordination and logistical assistance. The authors thank Kerry Lynch, geotechnical engineering technician at the University of Manitoba, for his assistance with the UAV.

7 REFERENCES

Abellán, A., Oppikofer, T., Jaboyedoff, M., Rosser, N. J., Lim, M., & Lato, M. J. (2014). Terrestrial laser scanning of rock slope instabilities. *Earth Surface Processes and Landforms*, *39*(1), 80–97. https://doi.org/10.1002/esp.3493

Barnhart, T. B., & Crosby, B. T. (2013). Comparing two methods of surface change detection on an evolving thermokarst using high-temporal-frequency terrestrial laser scanning, Selawik River, Alaska. *Remote Sensing*, *5*(6), 2813–2837. https://doi.org/10.3390/rs5062813

CloudCompare. (2018). CloudCompare (version 2.10) [GPL software]. Retrieved from http://www.cloudcompare.org/

Eltner, A., Kaiser, A., Castillo, C., Rock, G., Neugirg, F., & Abellán, A. (2016). Image-based surface reconstruction in geomorphometry-merits, limits and developments. *Earth Surface Dynamics*, *4*(2), 359–389. https://doi.org/10.5194/esurf-4-359-2016

Fonstad, M. A., Dietrich, J. T., Courville, B. C., Jensen, J. L., & Carbonneau, P. E. (2013). Topographic structure from motion: A new development in photogrammetric measurement. *Earth Surface Processes and Landforms*, *38*(4), 421–430. https://doi.org/10.1002/esp.3366

Harwin, S., & Lucieer, A. (2012). Assessing the accuracy of georeferenced point clouds produced via multi-view stereopsis from Unmanned Aerial Vehicle (UAV) imagery. *Remote Sensing*, *4*(6), 1573–1599. https://doi.org/10.3390/rs4061573

James, M. R., & Robson, S. (2012). Straightforward reconstruction of 3D surfaces and topography with a camera: Accuracy and geoscience application. *Journal of Geophysical Research: Earth Surface*, *117*(3), 1–17. https://doi.org/10.1029/2011JF002289

James, M. R., & Robson, S. (2014). Mitigating systematic error in topographic models derived from UAV and ground-based image networks. *Earth Surface Processes and Landforms*, *39*(10), 1413–1420. https://doi.org/10.1002/esp.3609

Kazhdan, M., Bolitho, M., & Hoppe, H. (2006). Poisson Surface Reconstruction. In *Eurographics Symposium on Geometry Processing*.

Lague, D., Brodu, N., & Leroux, J. (2013). Accurate 3D comparison of complex topography with terrestrial laser scanner: Application to the Rangitikei canyon (N-Z). *ISPRS Journal of Photogrammetry and Remote Sensing*, *82*, 10–26. https://doi.org/10.1016/j.isprsjprs.2013.04.009

Leica Geosystems. (2018). Leica Infinity. Heerbrugg, Switzerland. https://doi.org/10.1007/SpringerReference_28001

Meeks, C. T., Bonneau, D. A., Hutchinson, D. J., & Gauthier, D. (2017). The Use of Unmanned Aerial Vehicles (UAVs) for Slope Stability Assessment. In *GeoOttawa*.

Pix4D. (2018). Pix4Dmapper. Lausanne, Switzerland.

Rampton, V. N. (1980). *Quarternary Geology of the Tuktoyaktuk Coastlands, Northwest Territories*. *Geological Survey of Canada*.

senseFly. (2018). eMotion 3. Lausanne, Switzerland.

Stumpf, A., Malet, J. P., Allemand, P., Pierrot-Deseilligny, M., & Skupinski, G. (2015). Ground-based multi-view photogrammetry for the monitoring of landslide deformation and erosion. *Geomorphology*, *231*, 130–145. https://doi.org/10.1016/j.geomorph.2014.10.039

Tahar, K. N. (2013). An evaluation on different number of ground control points in unmanned aerial vehicle photogrammetric block. *International Archives of the Photogrammetry, Remote Sensing and Spatial Information Sciences - ISPRS Archives* (Vol. XL-2/W2, pp. 27–29). https://doi.org/10.5194/isprsarchives-XL-2-W2-93-2013

Westoby, M. J., Brasington, J., Glasser, N. F., Hambrey, M. J., & Reynolds, J. M. (2012). “Structure-from-Motion” photogrammetry: A low-cost, effective tool for geoscience applications. *Geomorphology*, *179*, 300–314. https://doi.org/10.1016/j.geomorph.2012.08.021